Acta Pharmaceutica Sinica B 2024;14(6):2669–2684

Chinese Pharmaceutical Association
Institute of Materia Medica, Chinese Academy of Medical Sciences

Acta Pharmaceutica Sinica B

www.elsevier.com/locate/apsb
www.sciencedirect.com

ORIGINAL ARTICLE

An emerging terpolymeric nanoparticle pore former as an internal recrystallization inhibitor of celecoxib in controlled release amorphous solid dispersion beads: Experimental studies and molecular dynamics analysis

Jamie Anne Lugtu-Pe[a,†], Xuning Zhang[a,b,†], Sako Mirzaie[a,†], Hao Han R. Chang[a], Nour AL-Mousawi[a,c], Kuan Chen[a], Yongqiang Li[b], Anil Kane[d], Daniel Bar-Shalom[c], Xiao Yu Wu[a,*]

[a]*Advanced Pharmaceutics and Drug Delivery Laboratory, Leslie Dan Faculty of Pharmacy, University of Toronto, Toronto M5S 3M2, Canada*
[b]*Candoo Pharmatech Company Inc., Mississauga L5N 5M1, Canada*
[c]*Department of Pharmacy, University of Copenhagen, Copenhagen DK-2100, Denmark*
[d]*Patheon by Thermo Fisher Scientific, Toronto Region Operations (TRO), Mississauga L5N 3X4, Canada*

Received 29 December 2023; received in revised form 25 January 2024; accepted 8 February 2024

KEY WORDS

Controlled release amorphous solid dispersion;
Poorly soluble drug;
Internal recrystallization;
Membrane-reservoir coated beads;
Molecular dynamics simulation;
Effect of pore formers;

Abstract Solid oral controlled release formulations feature numerous clinical advantages for drug candidates with adequate solubility and dissolution rate. However, most new chemical entities exhibit poor water solubility, and hence are exempt from such benefits. Although combining drug amorphization with controlled release formulation is promising to elevate drug solubility, like other supersaturating systems, the problem of drug recrystallization has yet to be resolved, particularly within the dosage form. Here, we explored the potential of an emerging, non-leachable terpolymer nanoparticle (TPN) pore former as an internal recrystallization inhibitor within controlled release amorphous solid dispersion (CRASD) beads comprising a poorly soluble drug (celecoxib) reservoir and insoluble polymer (ethylcellulose) membrane. Compared to conventional pore former, polyvinylpyrrolidone (PVP), TPN-containing membranes exhibited superior structural integrity, less crystal formation at the CRASD bead surface, and greater extent of celecoxib release. All-atom molecular dynamics analyses revealed that in the presence of TPN,

*Corresponding author.
E-mail address: sxy.wu@utoronto.ca (Xiao Yu Wu).
†These authors made equal contributions to this work.
Peer review under the responsibility of Chinese Pharmaceutical Association and Institute of Materia Medica, Chinese Academy of Medical Sciences.

https://doi.org/10.1016/j.apsb.2024.03.026

Terpolymer nanogel;
Drug-polymer interactions

intra-molecular bonding, crystal formation tendency, diffusion coefficient, and molecular flexibility of celecoxib were reduced, while intermolecular H-bonding was increased as compared to PVP. This work suggests that selection of a pore former that promotes prolonged molecular separation within a nanoporous controlled release membrane structure may serve as an effective strategy to enhance amorphicity preservation inside CRASD.

1. Introduction

Controlled release (CR) is a valuable formulation strategy, boasting benefits such as improved dosing regimen, increased efficacy, and reduced side effects, translating to better patient compliance and treatment success[1−3]. However, approximately 70%−90% active pharmaceutical ingredients (API) in development present poor water solubility and/or poor permeability, belonging to the Biopharmaceutic Classification System (BCS) Classes II and IV categories; hence, due to dissolution-rate limited bioavailability, development into an oral controlled release dosage form remains a challenge[4,5]. To address this, CR systems using amorphized drug have been emerging in literature[3,6−13]. Amorphization, typically achieved by solvent evaporation or melt quenching techniques[8,14−18], can drastically enhance the solubility of BCS Class II and IV API by disrupting the crystal lattice structure and solidifying the API molecules in an irregular (*i.e.*, amorphous) arrangement within polymer carriers. By lowering its thermodynamic stability, the API can dissolve more rapidly and reach concentration levels multiple times over its crystalline saturation. On the other hand, conventional (immediate release) amorphous solid dispersion (ASD) applications may be limited by such precipitous release, as they can be prone to recrystallization after very high rates[19] and extents[20] of supersaturation. If significant precipitation occurs prior to adequate absorption, the solubility advantage becomes clinically irrelevant. Hence the benefits of pairing CR with amorphization to create controlled release amorphous solid dispersions (CRASDs) are two-fold: (1) to extend CR benefits to a wider breadth of newly discovered drugs in addition to those existing drugs, which have been limited to immediate release formulation, and (2) to tailor release such that excessive, rapid supersaturation followed by recrystallization can be avoided.

Research in the field of ASD has predominantly portrayed drug recrystallization as a deleterious event initiating in the surrounding bulk dissolution media following supersaturation, usually manifested as a downward slope in the concentration versus time profile. However, emerging literature forewarns that precipitation within the dosage form merits greater attention when the ASD must be exposed to aqueous media for long periods (*i.e.*, CRASD)[21−23]. If internal precipitation is excessive, the rate and total amount of API release may be clinically inadequate; therefore, strategies to mitigate this phenomenon are essential to advance the application of CRASD in drug product development.

In our previous work, fluid-bed coating of membrane-reservoir coated beads was explored as an industrially relevant method to manufacture CRASD[10,24]. Operating on the same principle as spray drying, an ASD layer can be formed over an inert substrate, followed by application of a release-modifying membrane coating[7,9,10,12,24,25]. We proposed that the CR membrane plays an important role in counterbalancing supersaturation build-up in the bulk solution and within the dosage form, which can be achieved by tailoring permeability (thus release rate) with pore former concentration and coating level, but also by maximizing the capacity of the CR membrane to serve as a transient safe zone for drug *en route* to the bulk solution[24]. By promoting separation of drug molecules within an environment of relatively lower molecular mobility and higher affinity to polymers than in the medium, crystal formation may be inhibited within the membrane. In other studies, loading drug into carbon nanotubes, mesoporous silica and calcium carbonate featuring pores smaller than 50 nm have been reported to support pore-induced amorphization by preventing drug from assembling into any long-range order[26−28]. Hence, selection of materials to promote separation of drug molecules into nanostructured domains of amorphous drug within the CR membrane during dissolution appears to be one potential formulation approach to circumvent internal recrystallization.

Herein we explored the potential application of a cross-linked, amphiphilic terpolymer nanoparticle (TPN) composed of poly(-methacrylic acid)-polysorbate 80-*grafted*-starch (PMAA-PS80-*g*-St)[29] as an internal recrystallization inhibitor in CRASD beads. The TPN, exhibiting multifunctionalities, can be tuned in composition according to various applications (*e.g.*, nanoparticle carrier for injectable drugs, enteric coating excipient, and local pH modifier)[29−32]. Compared to conventional, water soluble polymeric pore formers, TPN resulted in lower viscosity of coating suspension, higher film integrity, homogenous distribution in the film and negligible leaching as a pore former in ethylcellulose (EC) coatings due to its miscibility in suspension and structural compatibility with EC[32]. Rather than forming water-filled channels for drug diffusion by leaching out[33,34], TPN remains embedded within the membrane, maintaining nano-scale pores formed by its swelling upon hydration[32]. Hence in this work, we investigate for the first time whether the sustained, nanoscaled pores of TPN, its enduring presence within an EC membrane as a unique performer, and potential molecular interaction with model drug, celecoxib (CEL), would enable the CRASD bead design to prolong amorphicity, prevent onset of recrystallization within the dosage form, and improve the attainable extent of drug release. Formulation factors on drug release from and recrystallization inside CRASD beads were evaluated both experimentally and theoretically. Molecular dynamics (MD), a Newtonian computational method[35−39], was exploited to delineate the molecular interactions of CEL with pore former polymers and the nanostructure of cross-linked TPN in relation to CEL mobility and alignment that contribute to the internal recrystallization tendency. This work has demonstrated that the composition and structure of a pore former in CR coating can be designed to maintain amorphous drug inside CRASD thereby enhancing the extent of release of poorly water-soluble drugs.

2. Materials and methods

2.1. Materials

CEL was received as a sample from AARTI Drugs Ltd., Mumbai, India. Microcrystalline cellulose beads (VIVAPUR® MCC Spheres 700), used as the coating substrate, were purchased from JRS Pharma (Weissenborn, Germany). Polyvinylpyrrolidone (PVP K30) and EC aqueous dispersion (Surelease® E−7-19040) were kindly donated by Colorcon (West Point, PA, USA). TPN was synthesized using soluble corn starch, methacrylic acid (MAA), *N*,*N*′-methylenebisacrylamide (MBA), sodium thiosulfate, potassium persulfate, and sodium dodecyl sulfate (SDS), purchased from Sigma−Aldrich (Oakville, ON, Canada), and polysorbate 80 (PS80) (Tween 80-LQ-(CQ)), donated by Croda (Edison, NJ, USA). Crystalline CEL formulation, Celebrex® capsules (100 mg), purchased for research purposes from Rexall Pharmacy (Mississauga, ON, Canada).

2.2. Synthesis, purification, and characterization of TPN

TPN synthesis and purification was scaled-up (10 ×) based on an aqueous free radical polymerization protocol previously developed[28]. Polymerization was performed in a condenser-attached 2000 mL three-necked round bottom flask immersed in a temperature-regulated water bath. Soluble corn starch (13.44 g) was pre-dissolved in 1440 g of distilled de-ionized water (DDIW), stirred at 90 °C for 30 min, then cooled to 65 °C and purged with nitrogen for 30 min. The initiators, sodium thiosulfate (1.44 g) and potassium persulfate (1.20 g), were then added to the solution and stirred under a nitrogen blanket. After 10 min, nitrogen purged 150 mL of solution of 16 g of MAA and 4 g MBA in DDIW and 150 mL solution of 2 g of SDS and 6 g of PS80 in DDIW were introduced to the flask. The reaction continued at 65 °C overnight with magnetic stirring. The mixture was then neutralized to pH 7 using ∼70 mL 2 N NaOH to prevent aggregation and settling of the formed polymer.

To purify the product, 20 mL volumes of TPN dispersion were washed with 30 mL ethanol in 50 mL Falcon tubes using an orbital shaker for 30 min. Tubes were centrifuged (Sorvall ST8 Benchtop Centrifuge, HIGH Conic III rotor (R = 120 mm), Thermo Scientific) for 20 min at 6500 RPM (2834×g), and pellets were collected in a beaker containing DDIW. Pellets were disintegrated using a high shear homogenizer (PowerGen 1000 S1, Fisher Scientific, Germany) and stirred until a stable suspension was formed. A second wash was performed using 12 mL of the suspension and 30 mL ethanol as per the conditions above. Following centrifugation, pellets were spread into a thin layer on weighing dishes to partially air-dry. Using a mortar and pestle, material was ground to a free-flowing powder and air-dried until no further weight loss on drying.

2.3. Dynamic light scattering

The intensity-weighted hydrodynamic particle size (*Z*-average), size distribution (polydispersity index, or PDI) and ζ potential of TPN were determined using a Malvern Zetasizer Nano ZS (Westborough MA). Sample concentrations of 0.05 mg/mL TPN in a pH 7 phosphate buffer (66 mmol/L) were mixed and sonicated using an ultrasonic probe sonicator (Hielscher UP100H, Teltow, Germany) prior to triplicate measurements using a folded capillary cell at 25 °C.

2.4. Water uptake and pore former leachability in free-films

To compare the pore-formation mechanism, distribution, and CEL uptake/distribution within the CR membrane, films were cast using 10% *w*/*w* of TPN or PVP in EC. Dispersions were prepared by combining 0.1 g of TPN or PVP with 4 g of Surelease® (25% aqueous dispersion containing EC), diluted to 11% *w*/*w* solids content with DDIW, stirred overnight, and sonicated with a probe sonicator (for mixtures containing TPN only) prior to casting onto tetrafluoroethylene evaporating plates. Samples were placed in a vacuum oven to degas at 30 mmHg for 20 min then dried overnight at 50 °C.

To measure water uptake (% uptake) and leachability (% weight loss) of the pore formers from the free-films, circular disk samples of uniform thickness and diameter were obtained using a 3/4" diameter die punch and were weighed before (w_0), after immersion in aqueous media (w_s), and after subsequent drying (w_d). Disks were incubated in 40 mL of pH 6.8 phosphate buffer in 50 mL Falcon tubes and shaken horizontally overnight at 37 °C, then dried in an oven at 45−50 °C for 24 h. Water uptake percentage was calculated as in Eq. (1):

$$\text{Water uptake}\ (\%) = \frac{w_s - w_0}{w_0} \times 100 \quad (1)$$

Weight loss percentages were calculated as per Eq. (2) given below:

$$\text{Weight loss}\ (\%) = \frac{w_0 - w_d}{w_0} \times 100 \quad (2)$$

2.5. Crystal detection by polarized light microscopy

To evaluate the pore distribution and physical state of CEL within the membrane, disk samples were soaked in 40 mL pH 6.8 media together with ASD beads containing CEL-PVP (prepared as described below) such that films were ∼10% of the total material weight, then incubated at 37 °C under agitation overnight. Films were rinsed with DDIW and patted dry to remove surface debris, then evaluated under polarized light microscopy (PLM) fitted with a full wave retardation plate to evaluate membrane appearance and detect birefringence (Motic BA400, Richmond, BC, Canada). PLM was also used to detect birefringence at the surface of CRASD beads during dissolution studies.

2.6. Preparation of CRASD membrane-reservoir beads by fluid-bed coating

Fluidized-bed coating using a bottom-spray Wurster assembly (Pro-C-ept 4M8 Fluid Bed, Zele, Belgium) was used to prepare bilayer CRASD beads with an inner ASD layer applied over inert MCC bead substrates, followed by an outer CR membrane layer. To achieve the first layer (ASD layer), a master batch of MCC substrates was spray-dried with a 10% (*w*/*w*) ethanolic solution of CEL-PVP (1:1) to 1.6% drug load, which was subsequently aliquoted into smaller batches for downward processing into CRASD beads. CRASD batches were formulated to contain 5% pore former (PF5%) and 10% pore former (PF10%) (*i.e.*, PVP or TPN), based on solids total weight, then coated to target levels of 2%, 4%, 6% and 9% weight gain (WG) (based on initial ASD beads weight). % WG was defined as the theoretical mass of coating solids applied over the initial mass of ASD substrate, based on the amount of coating solution used.

Surelease® coating dispersions were prepared as described above for film-casting. Spray coating parameters are presented in Table 1.

2.7. Dissolution studies

Dissolution studies were conducted using a USP Dissolution Apparatus II (VK 7000 Edison, NJ, USA), configured with a multi-cell UV−VIS spectrophotometer (Agilent Cary 8454, Waldbronn, Germany) and a multi-channel peristaltic pump (Ismatec ISM 931A, Idex, Oak Harbor, WA) to record CEL absorbance (λ = 255 nm). Sampling cannulas were fitted with 10 μm polytetrafluoroethylene filter tips (QLA, Telford, PA, USA). Beads equivalent to a dose of 40 mg CEL were tested in 900 mL of USP standard phosphate buffer pH 6.8 dissolution media maintained at 37.0 ± 0.5 °C agitated at 100 RPM. Since the pK_a of CEL (pK_a = 11.2) is much higher than the physiological pH range (pH 1.2−7.4), variance in its solubility was expected to be negligible across pH, hence for this study, the effect of TPN and PVP on release/recrystallization was compared only at pH 6.8 USP phosphate buffer. Based on the profiles obtained for Celebrex® capsules (crystalline CEL formulation) tested for comparison, this corresponded to a sink index (SI) of 0.036 according to Eq. (3) for sink index introduced by Sun[40]:

$$\mathrm{SI} = C_s/(\mathrm{dose}\,/\,V) \tag{3}$$

where C_s is the equilibrium solubility of crystalline drug in the testing media, V is the volume of dissolution media, and dose is the amount of drug being tested in the media. Areas under the curve over 24 h were calculated and compared between PVP and TPN formulations.

2.8. Evaluation of CRASD surface morphology by scanning electron microscopy (SEM)

SEM images of the surface and cross section of the beads were obtained by FEI Quanta FEG 250 Environmental SEM/STEM (FEI, Hillsboro, OR, USA), to evaluate the surface morphology of dry beads and the extent of CR layer erosion during dissolution. Beads were sampled at 5 h and air dried thoroughly with nitrogen. Samples were mounted onto holders using double-sided tape and images were obtained at 5 kV.

2.9. Evaluation of drug−polymer interaction and crystallization tendency

2.9.1. Molecular dynamics (MD) simulation

MD simulation was used to help elucidate the molecular mechanisms of the effect of TPN over PVP on the mobility and crystallization tendency of CEL within the hydrated EC membrane in the absence of pore formers (CEL-free) and in the presence of PVP (CEL-PVP) or TPN (CEL-TPN). Based on the ratio extracted from previous NMR measurement[29], the molar ratio of methacrylic acid (MAA), corn starch, polysorbate 80 (PS80), and *N*,*N*′-methylenebisacrylamide (MBA) as a cross-linker used in the TPN was set as 67, 23, 1, and 10, respectively. TPN and PVP were constructed *in silico* using the LEAP module of AmberTools17 software, version 17.05 (LINUX, University of California, San Francisco, CA, USA)[41]. Five chains of TPN were constructed, each consisting of twenty-three monomers. Roughly the same number of atoms (~10,000 excluding solvent molecules) were assigned for both polymers, TPN and PVP, to produce comparable outputs. To simulate the diminishing concentration of PVP in the EC membrane due to leaching over time, two additional concentrations of PVP, medium (med) and low, were evaluated, which were 25% and 10%, respectively, of the initial (high) concentration. In each system, five CEL molecules were included.

Simulations were performed on a workstation equipped with RTX 3090 GPU and Linux 22.04 LTS. For MD simulations, Latest Optimized Parameters for Liquid Simulations (OPLS4)[42] in Desmond software[43] was employed. TIP3P water model was assigned as a solvent, and temperature and pressure were kept to 310 K and 1 bar, respectively. In all MD runs, Nose−Hoover chain thermostat and Martyna-Tobias-Klein barostat were applied. The nonbonded interactions during simulations were truncated at 9 Å. For a production run of 200 ns, MD simulations were performed in an isothermal-isobaric (NPT) ensemble.

The MD data were analyzed using Python scripts. The radius of gyration (R_g) intuitively allows to probe the magnitude of dispersion of the studied molecules. In this study, we calculated R_g values of Free-CEL and CEL in the presence of the pore formers using Eq. (4):

$$R_g = \sqrt{\frac{1}{N}\sum_{i=1}^{N}|r(i) - r_{\mathrm{center}}|^2} \tag{4}$$

where N is the total number of molecules, and $r(i)$ and r_{center} are the coordinates of the i_{th} molecule and the centre of mass, respectively.

The diffusion coefficient of CEL, an indication of movement of CEL through the polymers, was computed using an extra 100 ns MD simulation with isothermal-isovolumetric (NVT) ensemble, using Eq. (5):

$$D = \frac{1}{6}\mathrm{Lim}_{t=\infty}\frac{\mathrm{d}}{\mathrm{d}t}\langle|r(t) - r(0)|^2\rangle \tag{5}$$

where $\langle|r(t) - r(0)|^2\rangle$ is the mean-square displacement, and the angled brackets demonstrate an ensemble average, which is an average over all particles in simulation time[40]. The mean squared displacement (MSD) method was used to measure the average displacement of particles versus time, and the standard deviation was calculated based on the deviation from MSD.

Radial distribution function (RDF), $g(r)$, was employed to find a particle at distance "r" from another particle during MD simulation[44]. The RDF analysis was performed on the MD trajectory obtained from the simulation of all systems by using Eq. (6):

$$g(r) = \frac{\mathrm{d}n(r)}{4\pi^2\mathrm{d}r\frac{N}{V}} \tag{6}$$

Table 1 Fluid-bed spray coating parameters for ASD and CRASD coatings.

Spray coating parameter	ASD coating	CR coating
Vessel volume	4 L	1 L
Batch initial weight	1000 g	140−170 g
Inlet air speed	0.5 m^3/min	0.3 m^3/min
Product temperature	40−50 °C	30−40 °C
Nozzle orifice diameter	0.6 mm	0.4 mm
Atomization pressure	0.75−1.0 bar	0.75−1.0 bar
Spray rate	1.5 g/min	1.5 g/min
Drying temperature and time	25 min at 50 °C	15 min at 60 °C

where d$n(r)$ refers to the differential number of atoms, meaning an infinitesimally small number of atoms, located within a spherical shell of infinitesimal thickness dr, at a distance r from a reference atom, and N/V is the average number density of computing atoms in the focused space[44].

2.9.2. FTIR analysis

FTIR analysis with a Universal ATR Sampling Accessory (Spectrum Two, UATR Two, PerkinElmer, MA, USA) was performed to compare the uptake of CEL within TPN-EC and PVP-EC films and to examine potential molecular interactions between CEL and polymers on. Film and powder samples were scanned 32 times over the spectrum range of 4000 to 500 cm^{-1}.

MD simulations and collective observations from PLM, DSC, and SEM were used to interpret release and recrystallization behavior between PVP and TPN formulations.

2.9.3. DSC analysis

To assess amorphicity of CEL within the formulations, CEL-loaded films and physical mixtures containing 4% CEL were evaluated using DSC. To evaluate the effect of each polymer on the amorphicity/recrystallization tendency of CEL, binary physical powder mixtures of CEL with either TPN, PVP or EC in a 2:8 ratio (as used for MD simulations) were compared. Samples weighing 5−10 mg were sealed in standard aluminum pans and tested under three cycles (heating, cooling, reheating) from 30 to 200 °C at a rate of 10 °C/min. Empty pans were used as the reference. TA Universal Analysis software (TA Instruments, New Castle, DE) was used to integrate the endothermic and exothermic peak areas, corresponding to the enthalpies of fusion and crystallization.

2.10. Statistical analysis

Statistical significance between the sample data was determined by performing one-way ANOVA and *post-hoc* pairwise comparisons using the two-tailed Student's t-test assuming equal variances, with Bonferonni correction. Unless otherwise stated, all measurements were performed in triplicate ($n = 3$) with mean ± standard deviation (SD). Statistical significance was defined at an alpha level of 0.05 unless multiple comparisons were performed.

3. Results and discussion

3.1. TPN characterization, pore formation mechanism, and crystal formation within free-films

Analysis by DLS confirmed that the synthesized TPN material was monodispersed (PDI = 0.26) with small particle size (Z-average diameter = 226 nm), and capable of forming a stable colloidal dispersion (ζ-potential = −18.0 mV) in pH 7 aqueous phosphate buffer, which is consistent with its characterization from our previous works[32] indicating an effective scaled-up process.

Water uptake studies indicated that in the absence of any pore former, EC films took up significanly less media (<10%) compared to those prepared with TPN (∼40%) and PVP (∼30%) (Fig. 1A). The lack of significant change in dry film weight for TPN-EC films after immersion in aqueous media, compared to the blank EC, indicated that TPN pore formation could be attributed solely to its permanence and nanogel swelling mechanism; unlike PVP, which is known to leach from EC films, corroborated by the significant decrease in weight after drying (Fig. 1B). The effect of film swelling, leachability, and pore former distribution on the uptake and physical state of CEL within the free-films was evaluated using PLM.

PLM equipped with a full wave retardation plate was used to evaluate pore former distribution and to detect crystalline material within TPN-EC, PVP-EC, and EC free-films after incubation in media with CEL ASD beads (Fig. 1C). After hydration in blank media, PVP-EC films left behind larger voids after PVP leaching (transparent spots, Row ii), which became occupied with material after immersion with ASD beads (dark spots, Row iii), and subsequently formed visible crystals after air drying (birefringence, Row iv), where all areas of interest indicated with white arrows. TPN on the other hand, maintained a more uniform, translucent appearance due to greater and more uniform water uptake throughout the film, and no birefringence was observed (Rows ii−iv). Pure EC films immersed in media retained the same translucency as dry films (Rows i−iv) due to their higher hydrophobicity and lowest water uptake (Fig. 1A), however some birefringence was detected at the film edges. Although some dark spots could also be seen in EC, these were smaller in size and evenly distributed compared to PVP, likely resulting from the low inherent porosity by the plasticizer and anti-tacking agent in the EC dispersion formulation (Surelease®).

As anticipated, the formation of larger, irregular shaped voids in the PVP-EC films was likely due to lower miscibility of PVP in EC[9], where PVP may have concentrated and subsequently leached, acting as sites for supersaturation and nucleation, thus can be more prone to internal recrystallization of CEL. The maintenance of greater film opacity and smoothness of TPN-EC films is an indication of enhanced distribution of CEL within smaller diameter of pores (*i.e.*, below the optical resolution of the microscope), which supports our proposed mechanism of nano-distribution to inhibit recrystallization.

3.2. Release of CEL from CRASD beads with different pore formers

The crystalline CEL commercial formulation exhibited a saturation concentration of 1.6 μg/mL when tested under the same dissolution conditions as the test formulations. Fig. 2 portrays the release behaviour and area under the curve (AUC) values obtained from PVP versus TPN CRASD bead formulations at PF5% and PF10% content over increasing coating levels (2%, 4% and 6% WG), from 0 to 24 h.

Both CRASD formulations provided a modest ∼4- to 6-fold increase over crystalline CEL saturation concentration that could be sustained longer. The effect of pore former type was most significant at the higher pore former level (PF10%), where TPN formulations significantly sustained higher CEL concentrations (8.5−9.5 μg/mL) compared to PVP formulations (6.8−8.6 μg/mL) (Fig. 2D and E, $P < 0.001$ and $P < 0.01$, respectively). Furthermore, the advantage of TPN was also evident at the lowest coating level (2% WG), as this formulation appeared to impart the CR function despite the low weight gain and resisted bulk solution precipitation for 15 h, whereas PVP formulations reached high CEL concentration followed by a rapid decline, likely due to insufficient amount of coating and distribution of PVP to form a complete barrier for controlled release. According to percolation theory, a higher concentration of pore former would increase the

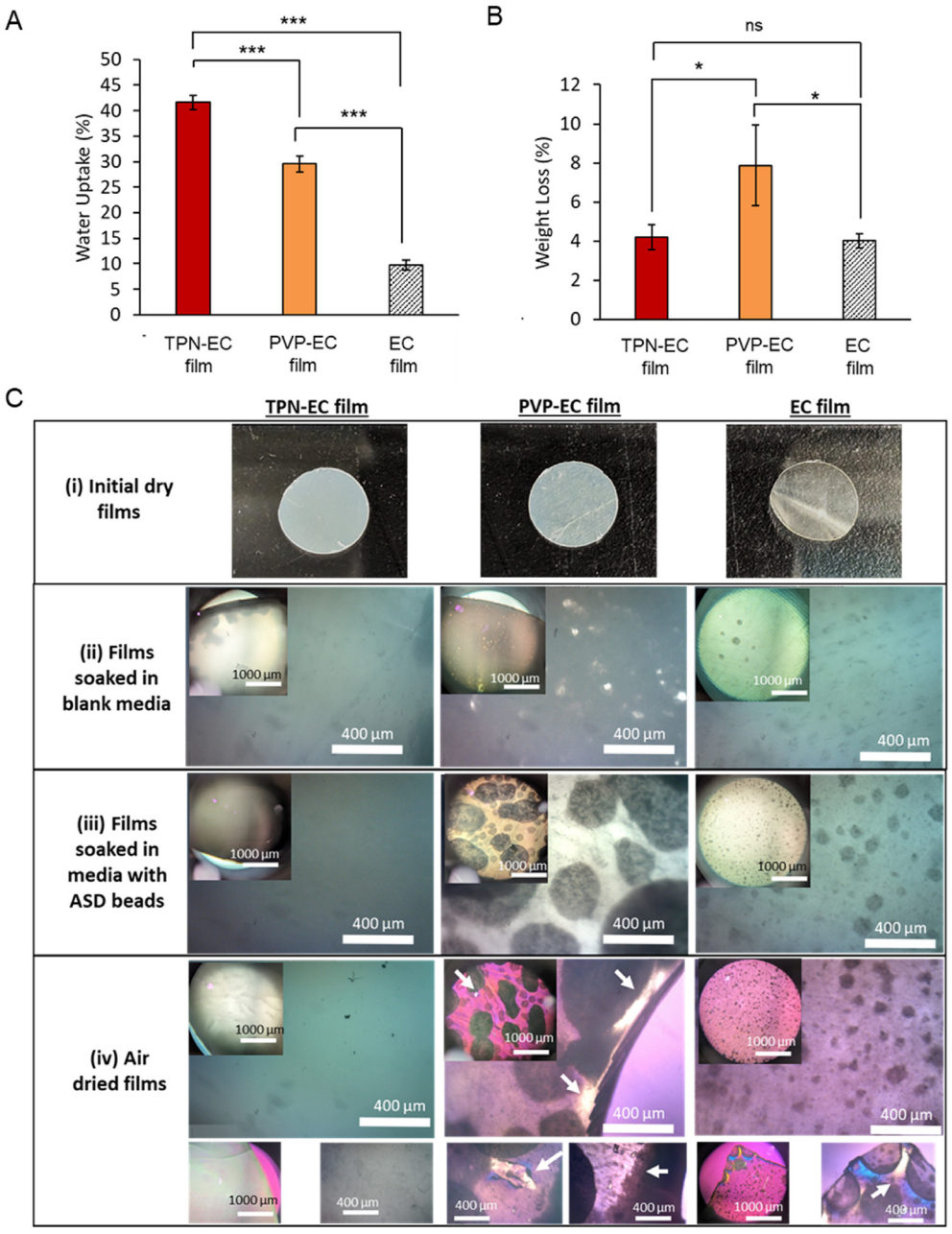

Figure 1 Comparison of water uptake (A), leachability (B), and pore distribution and crystal formation under PLM (C) within TPN-EC. PVP-EC and EC free-films. Data are mean ± SD, $n = 3$; ns $P > 0.05$ (not significant), $*P < 0.05$, $**P < 0.01$, $***P < 0.001$.

probability of forming sufficient interconnections of permeable channels to span the pathway along the membrane for drug to transport. For small molecules such as our model drug, CEL, percolation thresholds upwards of ~9% *w/w* have been estimated in porous polymer matrices, where pore forming materials with smaller size can function at lower thresholds[45,46]. Since TPN is dispersible on a finer scale, does not leach, and can swell significantly upon contact with water (Fig. 1A and B), narrower, longer nanochannels could indeed be formed at lower weight concentrations than PVP whch can explain its sustained effect in Fig. 2A. In contrast, PVP membranes would contain fewer, larger isolated pores lacking connectivity, serving as local precipitation sites preventing continual drug release. Moreover, PVP membranes may be weakened, permitting excessive water ingress to promote earlier onset and progression of internal recrystallization. Hence the ability of TPN to retain its CR function over a broader range of pore former and coating levels relative to PVP could be attributed to the polymers' respective size, dispersibility, and permanece in EC (Fig. 1).

When allowed to run beyond 24 h, release profiles of PVP and TPN formulations diverged further (Supporting Information Fig. S1A), exhibiting a notable decline in the measured bulk concentration for PVP. Since each measured timepoint is the net of drug recrystallization in the bulk solution and drug release, a downward slope indicates a relatively lower rate of drug release, which may signal the depletion of soluble drug reservoir. TPN

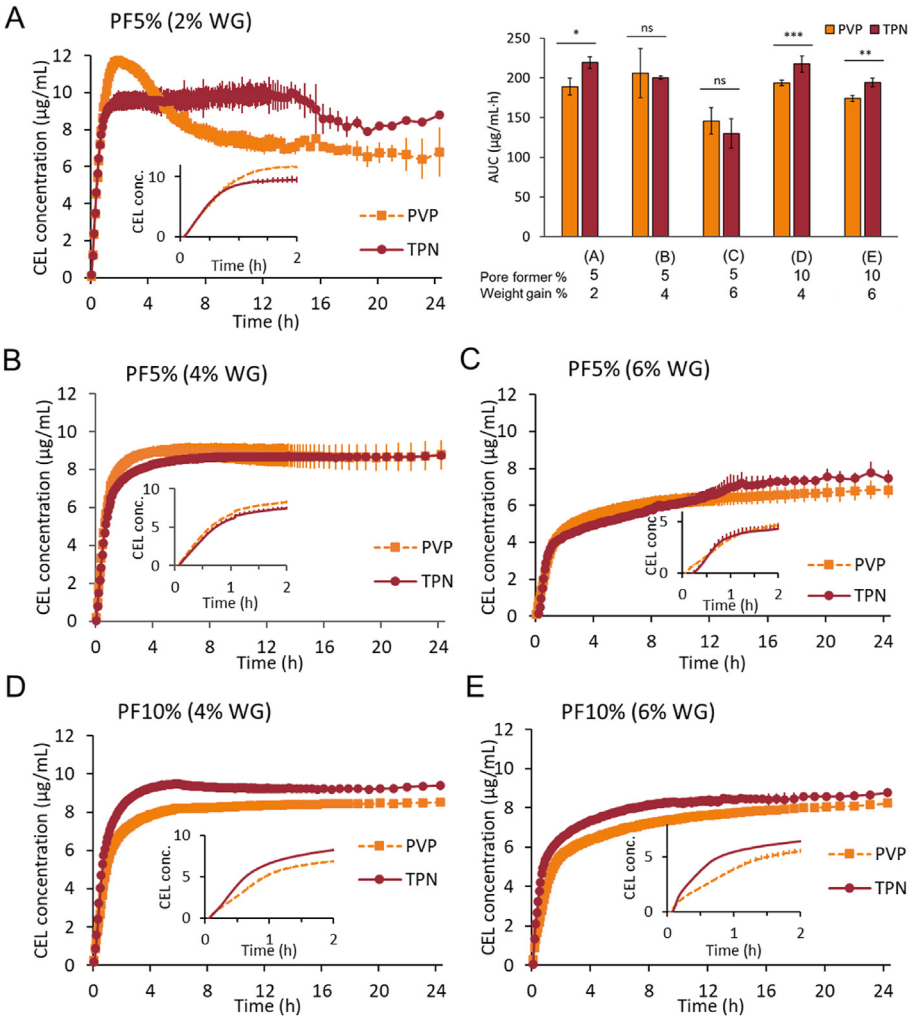

Figure 2 Release profiles and AUC of PVP *versus* TPN CRASD bead formulations at various coating levels (2%, 4%, and 6% WG) at 5% PF (A–C) and 10% PF (D, E) over 24 h. Data are mean ± SD, n = 3; ns, $P > 0.05$ (not significant), *$P < 0.05$, **$P < 0.01$, ***$P < 0.001$.

formulations, however, supported continual drug release up to 48 h, suggesting that drug remaining in the reservoir retained its amorphicity.

Slight concentration fluctuations were observed at ~30 h for PVP and TPN, which may be associated with the eventual loosening or detachment of the CR membrane from the bead core (Fig. S1), exposing the internal side of the CR membrane, inducing a greater surface area of the ASD layer to the dissolution media. TPN thus appeared to preserve the drug reservoir in the ASD layer and/or within the CR membrane (resulting in a jump in measured bulk concentration), whereas PVP became more susceptible to internal recrystallization by the greater influx of media (resulting in a decline). Although oral dosage forms are not intended to remain the GIT for such an extended period, the revelation that TPN membranes could sustain a longer driving force for release indicates greater robustness, which could be advantageous within a shorter timescale for situations or formulations more susceptible to internal recrystallization (*e.g.*, higher drug loadings, drugs with greater recrystallization tendency, more aggressive GIT conditions, after storage in high humidity and temperature, etc.)

3.3. Evaluation of CRASD bead membrane structural morphology and internal recrystallization by SEM and PLM

Representative SEM and PLM images of the CRASD beads sampled during dissolution studies are presented in Fig. 3.

Relative to the ASD beads (Fig. 3C), both formulations resulted in smooth, continuous films after the CR membrane application (Fig. 3A, $t = 0$ h, prior to immersion), and showed good adherance to the substrate and ASD layer (Fig. 3B, $t = 0$ h). However, PVP coatings deteriorated significantly more than TPN formulations over time, which is consistent with the qualititive observations of hydrated films and weight loss leachability studies (Fig. 1). The effect of pore former material type was most evident at 5 h, where TPN films appeared more continuous and intact, retaining a closer resemblance to beads prior to immersion; whereas PVP films proceeded to form visible ruptures and pores, laminate, and peel. This was evident in both the outer surface of the beads (Fig. 3A) and in the cross-sections (Fig. 3B).

Despite the ability of PVP to molecularly disperse (*i.e.*, dissolve) in water, it is reportedly immiscible with EC, as evidenced by retention of distinct glass transition values observed in

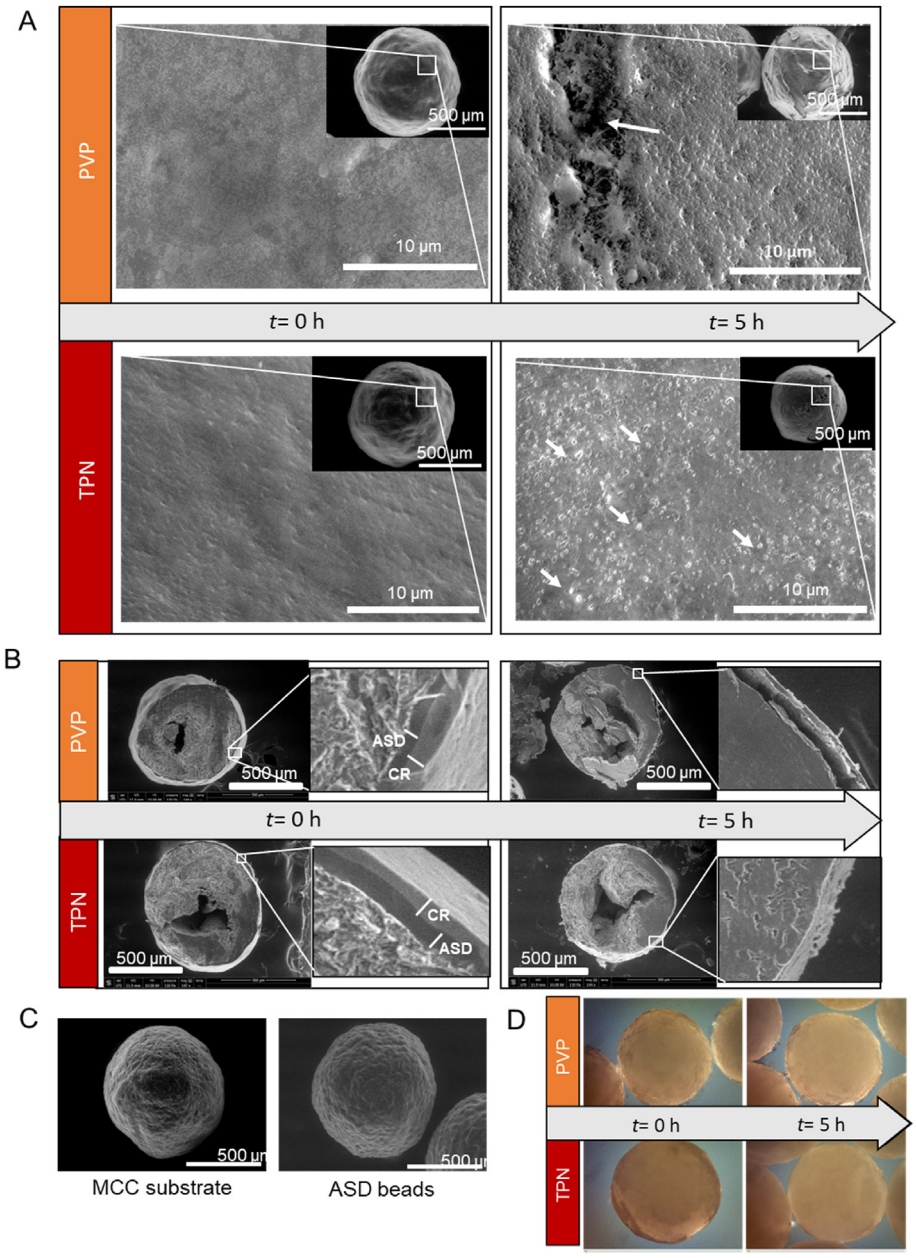

Figure 3 Representative images of CRASD beads containing 10% PF sampled during dissolution. (A) SEM images of CRASD bead surfaces; (B) SEM images of CRASD bead cross-sections; (C) SEM reference images of MCC bead substrate and ASD coated beads; (D) PLM images of CRASD beads.

modulated differential scanning calorimetry experiments[12]. Thus, PVP is likely more prone to segregate and create larger pores upon hydration and solution, as observed in our casted film experiments (Fig. 1C). This phenomenon can be inferred by the more prominent concavities and microscale pores (indicated by white arrows) observed on the magnified surfaces of PVP-EC films in Fig. 3A. The larger crevices could be indicative of film weakening due to bridging of the larger pores. Other studies have shown that films embedded with PVP resulted in pore sizes ranging from 0.35 to 0.64 µm[47,48]. This observation was consistent with our SEM experiments, revealing a micro-porous structure in the PVP-embedded EC, while the TPN exhibited pores below the resolution of the instrument, hence, could be estimated within the nanoscale (Fig. 3A, white arrows). The dimples found on the surface of our TPN formulations in the SEM images, represent particles or aggregates of the TPN embedded within EC. According to DLS, our current and previous works have shown the TPN particle size to range from 226 to 244 nm[32]. However, within the TPN particles, the gel mesh pore size upon swelling could be estimated to even smaller, which can be related to its cross-linking density. Based on the Lustig and Peppas Model, the swelling behavior of hydrogels can be adapted to estimate the average mesh size of the gel network based on factors such as cross-linking density[49]. Cross-linking density plays role in defining the spatial arrangement of polymer chains within the gel matrix, with higher cross-linking density leading to smaller mesh sizes[50-52]. Previously, our lab developed a xanthan gum-cross-linked starch that exhibited a gel mesh size ranging from 2.84 to 6.74 nm. The gel

mesh size range was achieved using 0%−20% sodium trimetha-phosphate (STMP) concentration relative to dry starch and calculated using the Lustig and Peppas theoretical model[51]. Thus, with 30% MBA as cross-linker in relation to dry starch for TPN, it is reasonable to expect the pores within the TPN network would also align within a comparable range (<10 nm). Within such narrow nanoporous dimensions, movement of the drug within the network would be restricted, which is beneficial to inhibit internal recrystallization.

Differences in coating texture were more noticeable when imaged after 48 h of dissolution (Fig. S1B, Supporting Information). The superior mechanical integrity of TPN in EC coated beads aligns with our previous study demonstrating an improved Young's modulus and tensile strength of TPN-containing EC membrane over prolonged exposure to dissolution media compared to other conventional pore-forming excipients[32]. As miscibility is not a prerequisite in conventional CR applications, PVP performs well in EC coating as a pore former[27,33]. However, in the case of this CRASD formualtion, the relatively less uniform and larger channels formed by PVP may have contributed to a faster depletion of amorphous drug reservoir compared to the more finely dispersed pores of TPN within the CR membrane.

Akin to free-films, beads with 10% pore former demonstrated greater birefringence at the bead surface of PVP formulation, suggesting more crystal formation compared to the TPN formulation (Fig. 3D and Fig. S1B). Although PVP is known to be an effective crystallization inhibitor of CEL in the solid state[53−55], due to its significant leaching into the media after 5 h of dissolution (Figs. 1B and 3A) (*i.e.*, leaving the vicinity of solid CEL), it no longer acts as an internal crystallization inhibitor within the bead. As a result, precipitation was apparent at the PVP bead surfaces (Fig. 3D). In contrast, smoother and more robust surface was observed under SEM and less birefringence under PLM on the membranes comprising TPN.

3.3.1. Analysis of CEL crystallization tendency and molecular interaction with pore formers

3.3.1.1. Molecular dynamics analysis. To help elucidate the molecular mechanisms governing the crystallization tendency of CEL within the EC membrane in the presence of water and pore formers, MD simulations were conducted with CEL in the absence (Free-CEL) and presence of the polymers (CEL-TPN, CEL-PVP (high, med, and low concentrations)). Over the course of 200 ns, various output parameters were monitored, including drug mobility, molecular flexibility (radius of gyration (R_g) and rotational dihedral angles), and interaction with the polymers (total binding energy, van der Waals (vdW), electrostatic, and hydrogen bond (H-bonds) interactions) (Figs. 4 and 5).

In the absence of polymers, recrystallization occurred for CEL molecules due to the formation of intra-H-bonds (Fig. 4A and 5C), which was consistent with previous experimental studies of the CEL crystal form[56]. Similar spatial alignment of methyl phenyl moieties was also observed in our simulated crystal. The study revealed that one facet of the CEL crystal exhibited increased hydrophillicity due to the presence exposed sulfamoyl moieties, while another facet was more hydrophobic due to the methyl phenyl moieties[56]. The molecular lipophilic surface potential analysis showed that sulfamoyl moiety exhibited a high tendency for interactions with the solvent molecules, thus facilitating CEL crystal formation and its stabilization[56]. Conversely, the methyl phenyl moiety has a higher lipophilicity, and thereby exhibited a

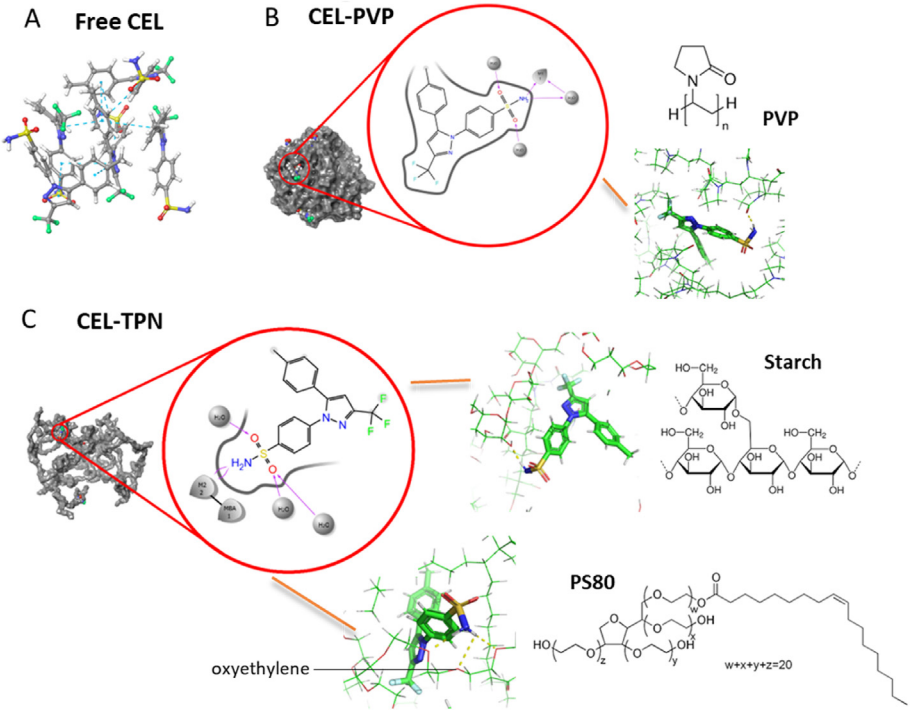

Figure 4 MD simulations of CEL in the absence and presence of polymer. (A) Interaction mode between CEL molecules; (B) Interaction mode between CEL-PVP and (C) CEL-TPN. Polymer structures are rendered by surface. Pyrrolidone and polyoxyethylene are represented by M1 and M2, respectively. H-bonds are shown by yellow dashed lines.

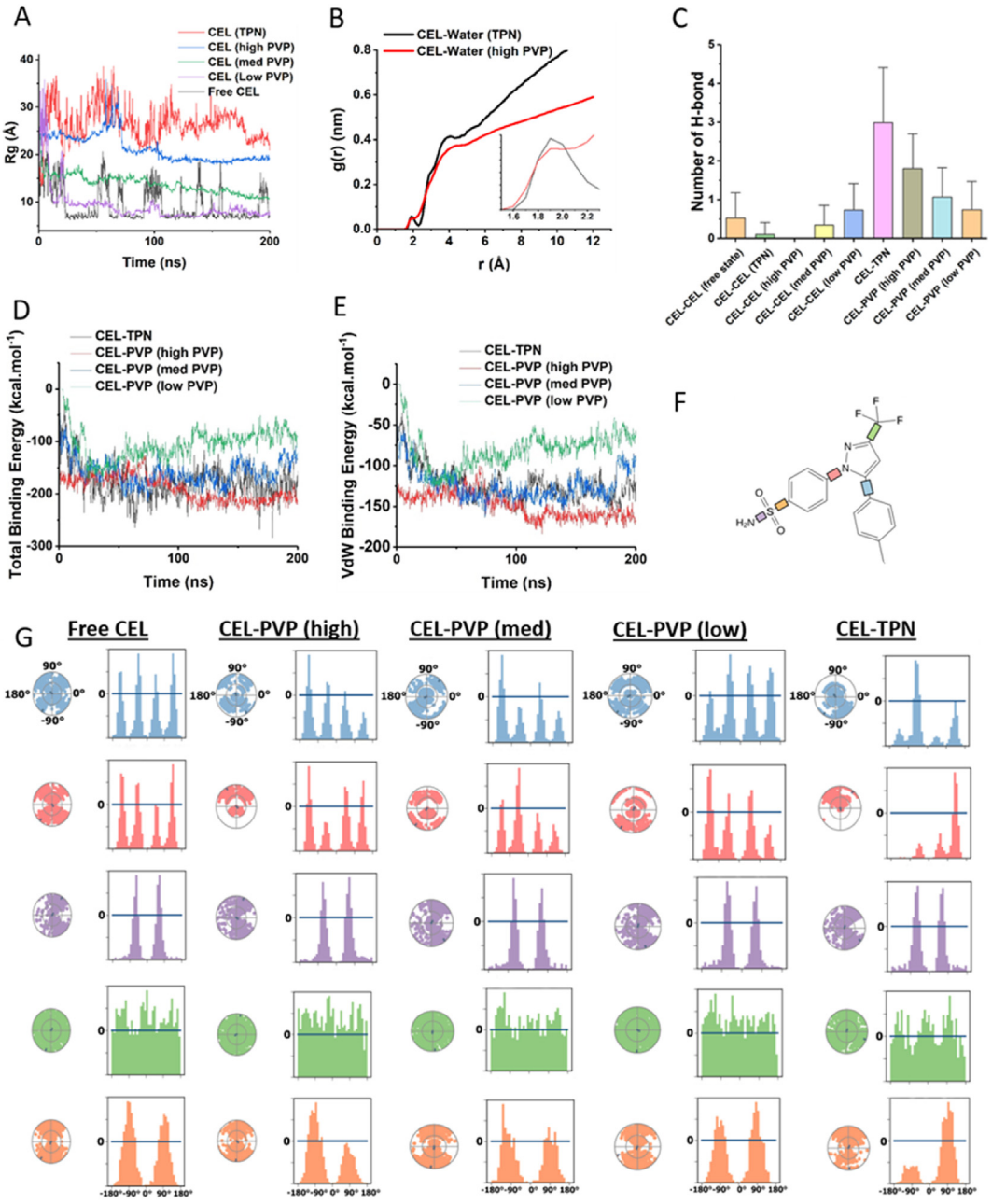

Figure 5 (A) Radius of gyration (R_g); (B) Radial distribution function (RDF); (C) Number of hydrogen bonds (H-bonds) between CEL and polymers (mean ± SD); (D) Total binding energy; (E) van der Waals (vdW) interaction energy; (F) CEL molecule indicating bonds of measured dihedral angle rotations; (G) Torsional conformation plots of CEL corresponding to the color of each rotatable bond shown in the CEL molecule.

weaker tendency to interact with the aqueous phase. In contrast, in the presence of polymers, CEL molecules became physically trapped, effectively preventing CEL recrystallization[56].

Following the cluster analysis, the average structures of CEL-PVP (high) and CEL-TPN complexes were identified (Fig. 4B and C). The NH_2 group of CEL molecule was observed to form a hydrogen bond with the carbonyl moeity of pyrrolidine ring from PVP (Fig. 4B), which is consistent with experimental findings in literature[57]. In addition, the MD simulation revealed the presence of two forms of hydrogen bonds between the TPN and CEL molecules; with the first H-bonds formed with PS80, and the second H-bonds were formed between the hydroxyl group of glucose, the repeating monomer unit of the starch backbone (Fig. 4C).

The average values of R_g for Free-CEL, CEL-PVP (high), CEL-PVP (med), CEL-PVP (low), and CEL-TPN were 9.44, 21.35, 13.82, 9.27, and 26.42 Å, respectively (Fig. 5A). The lower R_g values found with free CEL and at lower PVP concentration indicate higher compactness favoring recrystallization. Conversely, higher R_g values imply higher dispersion and

attachment of CEL within the polymer, which allows for more effective drug encapsulation and the formation of a more stable complex by the polymer[56].

Radial distribution function (RDF) analysis was conducted on MD trajectories to elucidate the number of interactions between CEL molecules and solvent. From the RDF analysis, a higher number of molecular interactions between the CEL and solvent molecules in the presence of TPN was observed (Fig. 5B). By decreasing the PVP concentration from high to low, the number of solvent molecules interacting with the CEL is also decreased (Supporting Information Fig. S2A). Hydrogen bonding, which is a dipole−dipole interaction and therefore considered a vdW force, was further supported as the dominant force of interaction between the CEL molecules and between the CEL and pore formers (Fig. 5C). The number of H-bonds between CEL molecules in three different states shows that molecular separation of CEL by both pore formers (TPN and high PVP), compared to the free state, drastically decreases the formation of intra-H-bonds. Moreover, the average number of H-bonds between TPN and CEL was 3.5, which was higher than H-bonding between CEL and high, med, and low levels of PVP (1.37, 0.98, and 0.81, respectively). The H-bonding between CEL molecules and TPN and high PVP during the 200 ns MD simulation is shown in Fig. S2B; and as shown in Fig. S2C, H-bonding interactions between CEL molecules gradually increased with decreasing the PVP concentration.

Fig. 5D and E presents total binding and vdW interaction energies, respectively, between CEL molecules and polymers, while Fig. S1 depicts the electrostatic interaction energy. The average total binding energy values between CEL molecules and TPN and PVP were −177.87 and −189.43 kcal/mol, respectively. The vdW interactions between CEL and PVP were stronger than that of CEL and TPN (Fig. 5E), however, the electrostatic interactions between drug molecules and TPN were stronger (Fig. S2D). These results confirmed that both polymers exhibit an affinity to CEL molecules, although by decreasing the PVP concentration (med PVP and low PVP), the vdW interaction energy and consequently total binding energy between CEL molecules and PVP polymers were elevated to −158.1 and −104.2 kcal/mol, respectively. Based on the MSD calculations, the diffusion coefficients computed for CEL in the presence of PVP and TPN polymers in aqueous media were 1.2×10^{-10} ($\pm 8.23 \times 10^{-14}$) m^2/s and 2.26×10^{-11} ($\pm 8.23 \times 10^{-14}$) m^2/s, respectively. The drastically lower diffusion coefficient of CEL in TPN could be explained by the stronger H-bond interactions, as shown in Fig. 5C. Therefore the magnitude of diffusivity, which affects both release and recrystallization rate, strongly depends on the selected polymer.

Further MD analyses were performed to evaluate the flexibity of CEL molecules in the absence and presence of TPN and PVP by measuring the rotational dihedral angles (Fig. 5F). The torsional conformations of each condition are shown in Fig. 5G. The polar plots illustrate the conformation of CEL as a function of time, where the radial coordinate is the simulation time, and the angular coordinate is the torsional angle. The bar charts indicate the probability of the torsions (average over time) as a function of angle. CEL has five rotatable bonds, where the primary difference in the five systems was found to be the torsions of three rotatable bonds: (1) the bond linking the pyrazole ring to the benzene ring (blue bond), (2) the bond linking the pyrazole ring to the benzene ring of benzenesulfonamide moiety (pink bond), and (3) the bond linking the benzene ring to the sulfonamide moiety (orange bond).

For free CEL, all three bonds (blue, pink, and orange) have the widest torsion (Fig. 5G). For the blue bond, the torsion fluctuation is slightly reduced in the presence of high PVP when compared with free CEL, which can be seen more clearly in the probabitlity bar plots. However, with decreasing PVP concentration (med PVP and low PVP), the bond fluctuation was elevated. In the presence of TPN, the bond fluctuation is highly restricted (−30° to −100°). For the pink bond, the torsion fluctuation is relatively restricted (20°−170°) in the presence of high PVP, and again, the torsion fluctuation increased with decreasing PVP concentration. In med and low PVPs, the torsion directions are almost opposite to the torsions in high PVP, causing their benzenesulfonamide rings to twist in opposite directions. This change in direction is crucial as it could decrease the probability of the formation of H-bond of the benzenesulfonamide moiety with the PVP polymer (Fig. 5C). Similarly, for the orange bond, the distribution regions of the five systems are also visibly different, with the torsion angle in the presence of TPN being the most restricted.

Based on the above analyses, the order of torsion fluctuation of the three bonds in the five different system is as follows: Free CEL > low PVP > med PVP > high PVP > TPN. Since greater flexibility of the CEL molecule increases the liklihood of conformation to $\pi-\pi$ stacking and makes H-bonding more amenable, the decreased frequency of angle rotations in presence of TPN further support its ability to restrict the alignment and stacking of CEL, inhibiting CEL recrystallization.

3.3.1.2. FTIR analysis. To discern the absence/presence of drug in the TPN formulations and to confirm the molecular interactions predicted by MD, FTIR analysis was performed using free-films incubated with CEL solution (Fig. 6).

Compared to the physical mixture (CEL-TPN-EC PM), which retained peaks at the same wavenumbers as CEL powder (3355, 3219, 3094, 1350, 1230, 1153 and 1130 cm^{-1}, indicated by the blue vertical dashed lines) there were slight shifts at 1235 and 1166 cm^{-1} in both TPN and PVP film samples (red vertical dashed lines), indicating molecular interaction after loading drug from the media. These wavenumbers correspond to stretching of the C−O in ethers (1235 cm^{-1}) and C−N (1166 cm^{-1}) bonds of the drug and polymers, which is consistent with our MD results.

Between the films prepared with TPN versus PVP, the greater intensity in CEL-TPN-EC films at these peaks, and others located near the peaks of CEL powder (*e.g.*, 1350 cm^{-1}) suggest greater interaction within the CEL-TPN-EC film compared to the CEL-PVP-EC film and/or greater presence of CEL. The difference in CEL peak intensities would be consistent with our expectation that there will be greater uptake and retention of CEL within TPN due to the greater water uptake and more restrictive gel network and molecular interaction, whereas less retention of CEL is expected within the larger pores of PVP-EC films after PVP has leached into the media.

In all blank films (*i.e.*, absence of CEL), a consistent peak at 1050 cm^{-1} was observed, corresponding to the characteristic ether (C−O) stretching of EC. When examining CEL-loaded PVP-EC films (CEL-PVP-EC), this peak resembled that of the PVP-EC film without CEL. However, in the CEL-TPN-EC film, a significant decrease in the peak intensity was noted, indicating the presence of intermolecular interactions. As there were no observable shifts in the blank films, it is likely that this interaction arises from the ether groups within the starch backbone or PS80 of TPN. The MD simulation results highlighted that the oxyethylene

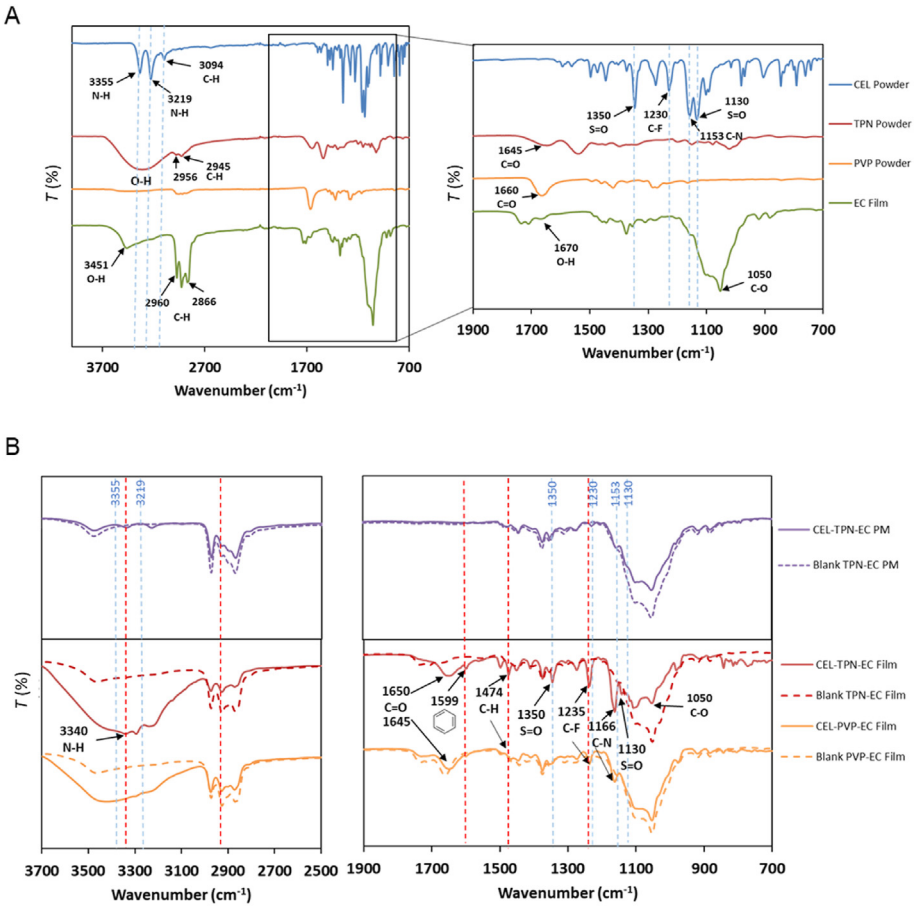

Figure 6 FTIR demonstrating molecular interaction between CEL and polymers. (A) Spectra of CEL, TPN, PVP, and EC; (B) Spectra of PM of CEL with TPN and EC (purple), TPN-EC film incubated with CEL (red) and PVP-EC film incubated with CEL. Blue dashed lines indicate characteristic peaks of CEL. Red dashed lines indicate peak intensities or shifts prominent in CEL-TPN-EC films.

groups in PS80, a component of the TPN polymer, interact with the NH2 groups of CEL. This interaction observed in the MD simulations aligns coherently with the findings from our FTIR data, showing a peak at 3340 cm^{-1}, corresponding to N−H stretching in secondary amines of CEL, providing a consistent understanding of the molecular interactions between the drug and polymer components. The appearance of a new peak at 1474 cm^{-1} related to C−H bending in CEL-TPN-EC film indicates changes in the hydrocarbon framework of the formulation, possibly due to the molecular rearrangement or proximity of CEL and TPN.

The emergence of a peak for aromatic carbons at 1599 cm^{-1} may reflect changes in the electronic environment of aromatic rings in CEL due to its interaction with TPN. A new peak for C−H stretching suggests alterations in the aliphatic chain environment, which could be a result of the physical proximity and interaction between CEL and TPN and PVP. Moreover, a peak at 1350 cm^{-1} was evident in the CEL-TPN-EC film, indicating the presence of oxygen in the sulfonamide group ($-SO_2NH-$) of CEL. This suggests potential hydrogen bonding between the sulfonamide and the ether group (C−O) in TPN-EC, due to the electronegative nature of oxygen and its tendency to form hydrogen bonds. This finding is consistent with MD simulations, affirming the molecular interaction of the sulfonamide group with the ether group of TPN.

Both PVP and TPN showed a peak at 1650 and 1645 cm^{-1}, respectively, indicating interaction involving the carbonyl group (C=O). These peaks potentially contribute to the amorphicity of CEL through hydrophobic VdW forces and/or hydrogen bonding with amine (NH_2) group of CEL. Notably, the strong peak at 1235 cm^{-1} in CEL-TPN-EC, in contrast to CEL-PVP-EC, suggests plausible hydrophobic interactions with the C−F groups of CEL with the hydrophobic segments of PS80. Furthermore, the spectrum exhibited an increase in intensity at peaks at 2960 and 2866 cm^{-1}, signifying alkane (C−H) stretching both CEL-loaded films (PVP and TPN) compared to the physical mixture. While PVP-EC displayed these similar interactions, TPN-EC exhibited a stronger interaction.

Overall, the FTIR findings aligns with other experimental results, highlighting how the capability of PVP and TPN in reducing CEL crystallinity. However, TPN demonstrates an additional, potentially stronger molecular interaction compared to PVP, offering TPN an advantage over PVP.

3.3.1.3. DSC analysis. The effects of molecular interaction of CEL with the polymers on its recrystallization tendency was also evaluated using DSC. Through the process of melting, it possible to observe changes in the crystallinity/amorphicity of drug before and after its molecular dispersion within a formulation. Hence the

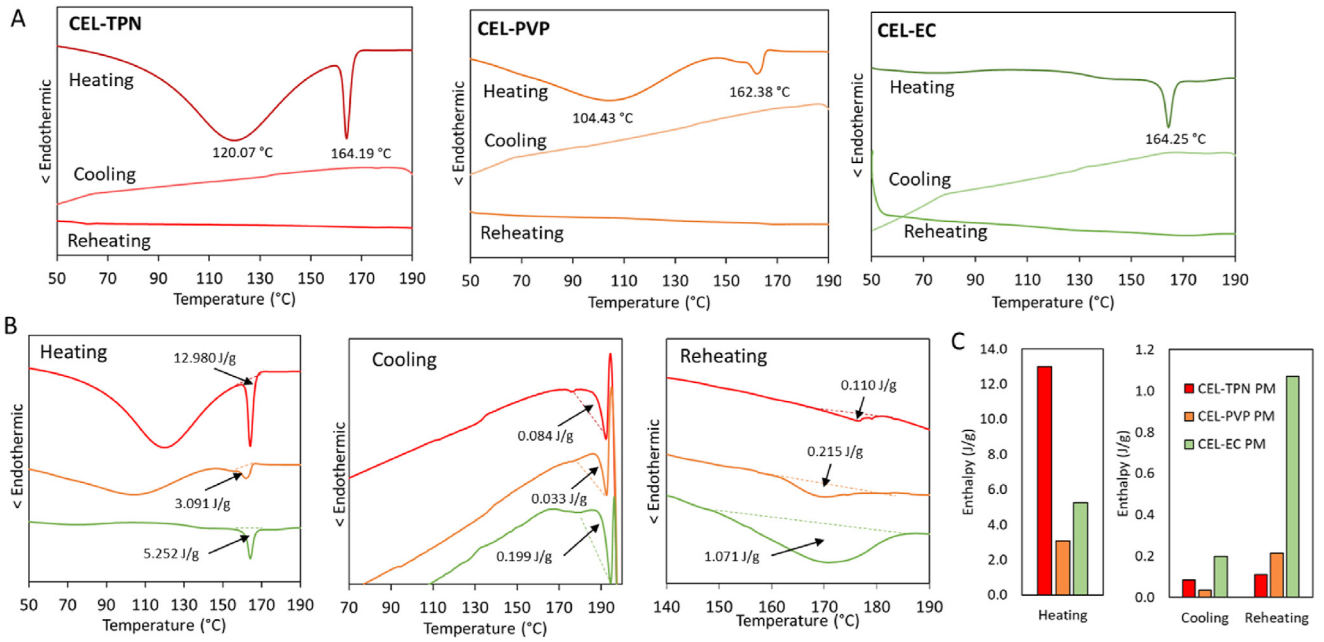

Figure 7 DSC thermograms of binary powder mixtures containing CEL and polymers, TPN, PVP, and EC. (A) Thermograms of each binary system over three cycles (heating, cooling, reheating) at 10 °C/min. (B, C) Comparison of enthalpies of fusion (heating and reheating cycles) and crystallization (cooling cycle) suggest improved recrystallization inhibition of CEL by TPN after initial heating.

thermal history of binary powder mixtures containing CEL with TPN, PVP and EC in the same ratio used for MD simulations (2:8) was tested over three consecutive cycles: heating, cooling, and reheating at 10 °C/min (Fig. 7).

On initial heating, crystallinity of CEL was evident in all powder mixtures, as expected, by the sharp endotherms at 164.19, 162.38, 164.25 °C for TPN, PVP, and EC samples respectively (Fig. 7A), corresponding to the known melting temperature of CEL at ∼165 °C. The larger CEL melting peak of CEL-TPN, relative to CEL-PVP and CEL-EC samples can be attributed to the lower T_g of starch (<90 °C)[58], cross-linked structure, and greater hygroscopicity of TPN, which is reflected by the preceding wide endotherm starting from ∼70 °C and extending through the MP of CEL. A greater amount of energy was likely required over a wider temperature range for the full transition of TPN to its molecular form and to remove any bound water, therefore molecular interaction with CEL could not be maximized until the end of the heating run. A wide endotherm also occurred with CEL-PVP between ∼70 and 140 °C, but to a lesser degree, followed by a shoulder and smaller melting endotherm of CEL, corresponding to the known T_g of PVP ∼149−171 °C[59], which allowed some molecular interaction during the initial run. Finally, CEL-EC also exhibited a relatively smaller endotherm compared to CEL-TPN on the initial heating run, which can be explained by the early T_g of EC (∼130 °C)[60] and greater opportunity to form hydrophobic interactions with CEL.

After complete molecular dispersion during the initial heating cycle, all samples became more amorphous (Fig. 7A), yet differences in the tendencies to partially recrystallize upon cooling could be detected by the lower enthalpies of crystallization in TPN (0.083 J/g) and PVP (0.033 J/g) samples compared to CEL in EC (0.199 J/g, Fig. 7B and C). This can be explained by the relatively stronger H-bonds formed between CEL and TPN and PVP (as predicted by MD), compared to the weaker hydrophobic interactions between CEL and EC, which facilitate greater resistance to the rearrangement of CEL crystals. Persistence of crystallinity is shown during the reheating cycle, where the enthalpy of fusion was greatest in CEL-EC (1.071 J/g), followed by CEL-PVP (0.215 J/g), compared to the negligible endotherm detected in TPN (0.110 J/g), thus supporting its greater advantage as a recrystallization inhibitor.

3.4. Proposed mechanism of amorphous CEL preservation in TPN membranes

Based on our experimental studies and MD simulations, the deviation in release behavior and internal drug recrystallization tendencies between CRASD beads formulated with PVP versus TPN were attributed to a triad of factors: (1) pore former distribution and (2) pore formation mechanisms within the EC-based CR membrane, and (3) molecular interaction with CEL. These key differenes affecting the CR membrane strucure, CEL distribution, and network restriction in the polymers are depicted in Fig. 8 to propose the mechanism of enhanced CEL amorphicity preservation in TPN formulations.

As portrayed in the diagram, TPN-EC membranes contain narrower and more numerous pores that are more uniformly distributed relative to PVP. Consistent with our SEM observations, the lower miscibility of PVP coarser distribution in the EC membrane resulted in larger, poorly defined pores after hydration and leaching. Conversely, TPN finely distributed in the membrane due to greater compatibility with EC, and formed higher amounts of nanoscaled channels inside upon swelling. It was proposed that decreasing the physical dimensions of the channels would restrict the rates of CEL movement and alignment, thereby reducing the susceptibility of CEL to form aggregates within the CR membrane. In addition, the nanoscaled channels would lead to a slower rate of ASD hydration, CEL dissolution, and local supersaturation

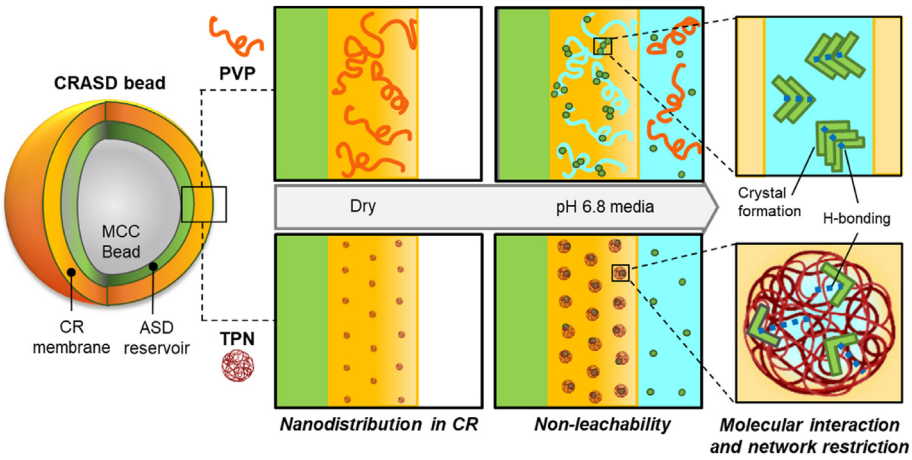

Figure 8 Proposed mechanism of CEL amorphicity preservation in TPN formulations.

beneath the membrane. Likewise, a higher proportion of ASD carrier could be retained for more congruent release with the drug, thus prolonging its function as a crystallization inhibitor.

From another aspect, slower hydration could allot more time for drug to partition into the CR membrane, which was recognized in our previous work with bilayer CRASD beads as a useful strategy to balance the relative rates of precipitation on either side of the membrane[24]. In our previous study, the CR membrane structure could be tailored with the proper selection of pore former concentration and coating level to create adequate points of entry and capacity to hold and transiently immobilize drug molecules, thereby acting as a temporary 'safe haven' for the amorphous drug. In the current study, since pores of the TPN were anticipated in the nanorange, capillary action could further facilitate CEL from the hydrated reservoir to enter the membrane, and subsequently distribute into and exit from the membrane in a more streamlined fashion. Since the channels formed by TPN were more numerous, this translated into greater number of entry points into the CR membrane from the ASD layer, ensuring more timely removal and prevention of supersaturation at the interface. In contrast, due to the fewer entry points in the PVP membranes, a bottle-neck effect may have prevailed, promoting local crystal formation, further blocking the passage sites.

In addition, molecular interaction between CEL and the CR membrane components is believed to further mitigate internal precipitation. Within the three-dimensional networks of TPN nanogel, interaction of drug with the wall of the pores would be thermodynamically preferred over crystal formation[26]. The nanoporous structure of TPN exposes numerous polymer chains and functional groups to prevent CEL aggregation by sterical hindrance and molecular interaction. As shown by MD simulations, the H−bond interaction between CEL and the pore formers indeed appears to prevent CEL crystal formation, with TPN showing a greater extent than PVP, particularly at lower PVP concentrations that mimick post leaching scenarios. Torsion angle analysis indicates that TPN highly restricts the three rotatable bonds in CEL. While high PVP also restricted the rotatable bonds, the decreasing PVP concentration led to increased torsion fluctuations, which can decrease the potential of drug molecules to form a H-bond with PVP polymer. The existence of more H-bonds btween TPN and CEL could decrease the diffusivity of CEL in aqueous media. Critically, the sustained presence of TPN in the membrane helps maintain the amorphous phase of CEL; whereas PVP leaching could create larger, water-filled domains that undesirably permit greater mobility and aggregation of drug molecules, expediting supersaturation and precipitation *in situ*. The issue of supersaturation and precipitation is especially problematic at lower pore former concentrations, where a lack of interconnections (*i.e.*, failure to percolate) to form continuous channels could result in isolated, ill-defined passageways and further impede drug release[34,45].

4. Conclusions

This work has revealed the important role of nanoporous structure and molecular interactions of a cross-linked amphiphilic nanoparticle, TPN, in the inhibition of internal recrystallization by MD simulation and experiments and demonstrated its usefulness as a unique poreformer to enhance the extent of drug release from a bilayered CRASD bead form of poorly water-soluble drugs. The results suggest that the non-leachable TPN can effectively inhibit internal recrystallization of CEL compared to a conventional water-soluble pore former, PVP, *via* its unique features and molecular interactions. Specifically, the refined and well-distributed nanoporous structure and the attractive molecular forces between CEL and TPN, determined by MD simulation and FTIR, promoted molecular separation of drug molecules within the networks of the nanogel and restricted mobility and allignment of drug molecules. Such multimodal effects enabled the regulation of drug release and inhibition of recrystallization process as observed *via* the release profiles and PLM. Unlike immediate release ASD formulations that require crystallization inhibitors dissolved in the medium to sustain supersaturation, advanced poreforming materials like TPN can maintain drug amorphicity within the CRASD forms. The results of this work suggest that utilizing such poreforming materials in CR membranes to prevent internal recrystallization is an effective strategy to address the spectrum of challenges posed by poorly water-soluble drugs. The integration of MD analyses with experimental studies enenables in-depth understanding and exploration of fundamental molecular and physical forces between drug and polymer (excipients) facilitating rational design of CRASD formulations of poorly soluble drugs.

Acknowledgments

This study was supported in part by an Ontario Research Fund-Research Excellence (ORF-RE) grant (Ontario, Canada) in

partnership with Patheon by Thermo Fisher Scientific, Natural Sciences and Engineering Research Council (NSERC) of Canada Discovery Grant and Equipment Grants to Xiao Yu Wu, University of Toronto (Canada), Leslie Dan Faculty of Pharmacy Dean's Fund to Jamie Anne Lugtu-Pe, University of Toronto (Canada), Mitacs Accelerate Internship sponsored by Candoo Pharmatech Company Inc. to Xuning Zhang (Canada), NSERC CREATE ContRoL program support to Sako Mirzaie and Hao Han R. Chang (Canada), Ontario Graduate Scholarship (OGS) to Hao Han R. Chang (Canada), and Pharmaceutical Sciences graduate department scholarships to Hao Han R. Chang and Kuan Chen, University of Toronto (Canada). The authors also sincerely thank Dr. Ping Lee for the use of DSC and polarized light microscope, University of Toronto (Canada), Dr. David Dubins for the use of the fluid bed coater in the Patheon Pharmaceutics Teaching Laboratory, University of Toronto (Canada), Colorcon for providing samples of PVP and Surelease® EC, Croda for donating PS 80, and Florent Vilotte (Colorcon) for providing technical advice on coating conditions.

Author contributions

Jamie Anne Lugtu-Pe conceptualized the idea, designed the research and formulations, performed the experiments, analyzed results, and wrote the main manuscript text. Xuning Zhang planned experiments, scaled-up the TPN synthesis and purification, casted films, coated beads, performed dissolution and microscopy studies, analyzed results, and wrote experimental sections of the manuscript. Sako Mirzaie performed the molecular dynamics (MD) simulations, analyzed MD results, and wrote the MD sections of the manuscript. Hao Han R. Chang prepared and characterized initial TPN compositions, performed FTIR and DSC analyses, and contributed writing and editing of the manuscript. Kuan Chen prepared and characterized initial TPN compositions, reviewed and edited the manuscript. Nour AL-Mousawi scaled-up the TPN synthesis and purification, characterized TPN and performed film-casting studies. Yongqiang Li provided analytical advice and review of the manuscript. Daniel Bar-Shalom and Anil Kane reviewed and edited the manuscript. Xiao Yu Wu conceptualized and supervised the project, analyzed results, reviewed, and edited the manuscript, and provided funding and resources. All authors have read and agreed to the published version of the manuscript.

Conflicts of interest

The authors declare no conflicts of interest.

Appendix A. Supporting information

Supporting data to this article can be found online at https://doi.org/10.1016/j.apsb.2024.03.026.

References

1. De Robertis S, Bonferoni MC, Elviri L, Sandri G, Caramella C, Bettini R. Advances in oral controlled drug delivery: the role of drug–polymer and interpolymer non-covalent interactions. *Expet Opin Drug Deliv* 2015;**12**:441–53.
2. Chen X, Wen H, Park K. Challenges and new technologies of oral controlled release. Chapter 16. In: Wen Hong, Park Kinam, editors. *Oral controlled release formulation design and drug delivery: theory to Practice*. New York: John Wiley & Sons, Inc.; 2010. p. 257–77.
3. Tran PHL, Tran TTD, Park JB, Lee BJ. Controlled release systems containing solid dispersions: strategies and mechanisms. *Pharm Res (N Y)* 2011;**28**:2353–78.
4. Ellenberger DJ, Miller DA, Williams IIIRO. Expanding the application and formulation space of amorphous solid dispersions with KinetiSol®: a review. *AAPS PharmSciTech* 2018;**19**:1933–56.
5. Chow K, Kane A. Parallel screening. *Eur Pharm Contract* 2011;**158**:100–4.
6. Cui F, Yang M, Jiang Y, Cun D, Lin W, Fan Y, et al. Design of sustained-release nitrendipine microspheres having solid dispersion structure by quasi-emulsion solvent diffusion method. *J Control Release* 2003;**91**:375–84.
7. Tran PH, Tran TT. Dosage form designs for the controlled drug release of solid dispersions. *Int J Pharm* 2020;**581**:119274.
8. Coppens KA, Hall MJ, Mitchell SA, Read MD. Hypromellose, ethylcellulose, and polyethylene oxide use in hot melt extrusion. *Pharmaceut Technol* 2006;**30**:62–70.
9. Dereymaker A, Pelgrims J, Engelen F, Adriaensens P, Van den Mooter G. Controlling the release of indomethacin from glass solutions layered with a rate controlling membrane using fluid-bed processing. Part 2: the influence of formulation parameters on drug release. *Mol Pharm* 2017;**14**:974–83.
10. Lugtu-Pe JA, Ghaffari A, Chen K, Kane A, Wu XY. Development of controlled release amorphous solid dispersions (CRASD) using polyvinyl acetate-based release retarding materials: effect of dosage form design. *Eur J Pharmaceut Sci* 2018;**124**:319–27.
11. Keen JM, Hughey JR, Bennett RC, Jannin V, Rosiaux Y, Marchaud D, et al. Effect of tablet structure on controlled release from supersaturating solid dispersions containing glyceryl behenate. *Mol Pharm* 2015;**12**:120–6.
12. Dereymaker A, Scurr DJ, Steer ED, Roberts CJ, Van den Mooter G. Controlling the release of indomethacin from glass solutions layered with a rate controlling membrane using fluid-bed processing. Part 1: surface and cross-sectional chemical analysis. *Mol Pharm* 2017;**14**:959–73.
13. Kaur A, Yadav JP, Sathe RY, Puri V, Bharatam PV, Bansal AK. Understanding poor milling behavior of voriconazole from crystal structure and intermolecular interactions. *Mol Pharm* 2022;**19**:985–97.
14. Boyd BJ, Bergström CA, Vinarov Z, Kuentz M, Brouwers J, Augustijns P, et al. Successful oral delivery of poorly water-soluble drugs both depends on the intraluminal behavior of drugs and of appropriate advanced drug delivery systems. *Eur J Pharmaceut Sci* 2019;**137**:104967.
15. Albers J, Alles R, Matthée K, Knop K, Nahrup JS, Kleinebudde P. Mechanism of drug release from polymethacrylate-based extrudates and milled strands prepared by hot-melt extrusion. *Eur J Pharm Biopharm* 2009;**71**:387–94.
16. Park J, Park HJ, Cho W, Cha KH, Kang YS, Hwang SJ. Preparation and pharmaceutical characterization of amorphous cefdinir using spray-drying and SAS-process. *Int J Pharm* 2010;**396**:239–45.
17. Paudel A, Worku ZA, Meeus J, Guns S, Van den Mooter G. Manufacturing of solid dispersions of poorly water soluble drugs by spray drying: formulation and process considerations. *Int J Pharm* 2013;**453**:253–84.
18. Song S, Wang C, Zhang B, Sun CC, Lodge TP, Siegel RA. A rheological approach for predicting physical stability of amorphous solid dispersions. *J Pharm Sci* 2023;**112**:204–12.
19. Sun DD, Lee PI. Evolution of supersaturation of amorphous pharmaceuticals: the effect of rate of supersaturation generation. *Mol Pharm* 2013;**10**:4330–46.
20. Han YR, Lee PI. Effect of extent of supersaturation on the evolution of kinetic solubility profiles. *Mol Pharm* 2017;**14**:206–20.
21. Purohit HS, Taylor LS. Phase behavior of ritonavir amorphous solid dispersions during hydration and dissolution. *Pharm Res (N Y)* 2017;**34**:2842–61.

22. Van Eerdenbrugh B, Raina S, Hsieh YL, Augustijns P, Taylor LS. Classification of the crystallization behavior of amorphous active pharmaceutical ingredients in aqueous environments. *Pharm Res (N Y)* 2014;**31**:969−82.
23. Saboo S, Mugheirbi NA, Zemlyanov DY, Kestur US, Taylor LS. Congruent release of drug and polymer: a "sweet spot" in the dissolution of amorphous solid dispersions. *J Control Release* 2019;**298**:68−82.
24. Lugtu-Pe JA, Lin BY, Chen K, Ghaffari A, Kane A, Wu XY. Tailoring release profiles of BCS class II drugs using controlled release amorphous solid dispersion beads with membrane-reservoir design: effect of pore former and coating levels. *Mol Pharm* 2021;**18**:4198−209.
25. Puri V, Dantuluri AK, Bansal AK. Barrier coated drug layered particles for enhanced performance of amorphous solid dispersion dosage form. *J Pharm Sci* 2012;**101**:342−53.
26. Forsgren J, Andersson M, Nilsson P, Mihranyan A. Mesoporous calcium carbonate as a phase stabilizer of amorphous celecoxib−an approach to increase the bioavailability of poorly soluble pharmaceutical substances. *Adv Healthcare Mater* 2013;**2**:1469−76.
27. Hacene YC, Singh A, Van den Mooter G. Drug loaded and ethylcellulose coated mesoporous silica for controlled drug release prepared using a pilot scale fluid bed system. *Int J Pharm* 2016;**506**:138−47.
28. Zhu W, Huang H, Dong Y, Han C, Sui X, Jian B. Multi-walled carbon nanotube-based systems for improving the controlled release of insoluble drug dipyridamole. *Exp Ther Med* 2019;**17**:4610−6.
29. Shalviri A, Chan HK, Raval G, Abdekhodaie MJ, Liu Q, Heerklotz H, et al. Design of pH-responsive nanoparticles of terpolymer of poly (methacrylic acid), polysorbate 80 and starch for delivery of doxorubicin. *Colloids Surf B Biointerfaces* 2013;**101**:405−13.
30. Chang HHR, Chen K, Lugtu-Pe JA, Al-Mousawi N, Zhang X, Bar-Shalom D, et al. Design and optimization of a nanoparticulate pore former as a multifunctional coating excipient for pH transition-independent controlled release of weakly basic drugs for oral drug delivery. *Pharmaceutics* 2023;**15**:547.
31. Shalviri A, Raval G, Prasad P, Chan C, Liu Q, Heerklotz H, et al. pH-Dependent doxorubicin release from terpolymer of starch, polymethacrylic acid and polysorbate 80 nanoparticles for overcoming multi-drug resistance in human breast cancer cells. *Eur J Pharm Biopharm* 2012;**82**:587−97.
32. Chen K, Chang HHR, Shalviri A, Li J, Lugtu-Pe JA, Kane A, et al. Investigation of a new pH-responsive nanoparticulate pore former for controlled release enteric coating with improved processability and stability. *Eur J Pharm Biopharm* 2017;**120**:116−25.
33. Yang M, Xie S, Li Q, Wang Y, Chang X, Shan L, et al. Effects of polyvinylpyrrolidone both as a binder and pore-former on the release of sparingly water-soluble topiramate from ethylcellulose coated pellets. *Int J Pharm* 2014;**465**:187−96.
34. Wang Y, Dai J, Chang X, Yang M, Shen R, Shan L, et al. Model drug as pore former for controlled release of water-soluble metoprolol succinate from ethylcellulose-coated pellets without lag phase: opportunities and challenges. *AAPS PharmSciTech* 2015;**16**:35−44.
35. Villalobos R, V Garcia E, Quintanar D, M Young P. Drug release from inert spherical matrix systems using Monte Carlo simulations. *Curr Drug Deliv* 2017;**14**:65−72.
36. Lopes D, Jakobtorweihen S, Nunes C, Sarmento B, Reis S. Shedding light on the puzzle of drug-membrane interactions: experimental techniques and molecular dynamics simulations. *Prog Lipid Res* 2017;**65**:24−44.
37. Bunker A, Róg T. Mechanistic understanding from molecular dynamics simulation in pharmaceutical research 1: drug delivery. *Front Mol Biosci* 2020;**7**:604770.
38. Maus M, Wagner KG, Kornherr A, Zifferer G. Molecular dynamics simulations for drug dosage form development: thermal and solubility characteristics for hot-melt extrusion. *Mol Simulat* 2008;**34**:1197−207.
39. Chan T, Ouyang D. Investigating the molecular dissolution process of binary solid dispersions by molecular dynamics simulations. *Asian J Pharm Sci* 2018;**13**:248−54.
40. Kamath A, Laha A, Pandiyan S, Aswath S, Vatti AK, Dey P. Atomistic investigations of polymer-doxorubicin-CNT compatibility for targeted cancer treatment: a molecular dynamics study. *J Mol Liq* 2022;**348**:118005.
41. Case D, Cerutti D, Cheatham IIIT, Darden T, Duke R, Giese T, et al. AMBER 2017 reference manual. 2017. Available from: https://ambermd.org/doc12/Amber17.pdf.
42. Román J, Castillo A, Mahn A. Molecular docking of potential inhibitors of broccoli myrosinase. *Molecules* 2018;**23**:1313.
43. Lu C, Wu C, Ghoreishi D, Chen W, Wang L, Damm W, et al. OPLS4: improving force field accuracy on challenging regimes of chemical space. *J Chem Theor Comput* 2021;**17**:4291−300.
44. Mehta CH, Narayan R, Aithal G, Pandiyan S, Bhat P, Dengale S, et al. Molecular simulation driven experiment for formulation of fixed dose combination of darunavir and ritonavir as anti-HIV nanosuspension. *J Mol Liq* 2019;**293**:111469.
45. Hastedt JE, Wright JL. Diffusion in porous materials above the percolation threshold. *Pharm Res (N Y)* 1990;**7**:893−901.
46. Zhang K, Wu XY. Temperature and pH-responsive polymeric composite membranes for controlled delivery of proteins and peptides. *Biomaterials* 2004;**25**:5281−91.
47. Godakanda VU, Li H, Alquezar L, Zhao L, Zhu LM, de Silva R, et al. Tunable drug release from blend poly(vinyl pyrrolidone)-ethyl cellulose nanofibers. *Int J Pharm* 2019;**562**:172−9.
48. Jiang J, Shen Y, Yu D, Yang T, Wu M, Yang L, et al. Porous film coating enabled by polyvinyl pyrrolidone (pvp) for enhanced air permeability of fabrics: the effect of pvp molecule weight and dosage. *Polymers* 2020;**12**:2961.
49. Lustig SR, Peppas NA. Solute diffusion in swollen membranes. IX. Scaling laws for solute diffusion in gels. *J Appl Polym Sci* 1988;**36**:735−47.
50. Canal T, Peppas NA. Correlation between mesh size and equilibrium degree of swelling of polymeric networks. *J Biomed Mater Res* 1989;**23**:1183−93.
51. Shalviri A, Liu Q, Abdekhodaie MJ, Wu XY. Novel modified starch−xanthan gum hydrogels for controlled drug delivery: synthesis and characterization. *Carbohydr Polym* 2010;**79**:898−907.
52. Naeem F, Khan S, Jalil A, Ranjha NM, Riaz A, Haider MS, et al. pH responsive cross-linked polymeric matrices based on natural polymers: effect of process variables on swelling characterization and drug delivery properties. *Bioimpacts* 2017;**7**:177−92.
53. Xie T, Taylor LS. Dissolution performance of high drug loading celecoxib amorphous solid dispersions formulated with polymer combinations. *Pharm Res (N Y)* 2016;**33**:739−50.
54. Gupta P, Kakumanu VK, Bansal AK. Stability and solubility of celecoxib-PVP amorphous dispersions: a molecular perspective. *Pharm Res (N Y)* 2004;**21**:1762−9.
55. Knopp MM, Nguyen JH, Becker C, Francke NM, Jørgensen EB, Holm P, et al. Influence of polymer molecular weight on *in vitro* dissolution behavior and *in vivo* performance of celecoxib: PVP amorphous solid dispersions. *Eur J Pharm Biopharm* 2016;**101**:145−51.
56. Modi SR, Dantuluri AK, Puri V, Pawar YB, Nandekar P, Sangamwar AT, et al. Impact of crystal habit on biopharmaceutical performance of celecoxib. *Cryst Growth Des* 2013;**13**:2824−32.
57. Shimpi SL, Mahadik KR, Paradkar AR. Study on mechanism for amorphous drug stabilization using Gelucire 50/13. *Chem Pharm Bull* 2009;**57**:937−42.
58. Liu P, Yu L, Liu H, Chen L, Li L. Glass transition temperature of starch studied by a high-speed DSC. *Carbohydr Polym* 2009;**77**:250−3.
59. Kolter K, Karl M, Gryczke A. *Hot-melt extrusion with BASF pharma polymers: extrusion compendium*. 2nd ed. Ludwigshafen: BASF; 2012 [Technical booklet].
60. Vesey C, Farrell T, Rajabi-Siahboomi A. Evaluation of alternative plasticizers for surelease®, an aqueous ethylcellulose dispersion for modified release film-coating [poster reprint]. *CRS Annual Meeting* 2005.